NIP TOMOGRAPHY REVISITED – FROM REFLECTIONS TO DIFFRACTIONS

A. Bauer, B. Schwarz, M. Lotze, T. Werner, and D. Gajewski

email: *alex.bauer@uni-hamburg.de*

keywords: *diffractions, tomography, zero-offset, inversion, CRS*

ABSTRACT

The common-reflection-surface (CRS) stack was shown to be a powerful tool for data analysis and enhancement. While the increased signal-to-noise ratio and the regularization and interpolation capabilities are virtues on their own, the physically meaningful attributes acquired during the CRS stack can be used for sophisticated subsequent processes such as wavefield characterization and separation. In this work, we review the largely data-driven normal-incidence-point (NIP) tomography, which likewise makes use of the CRS parameter estimates. Whereas in previous works, NIP tomography has been applied mainly to reflection data, resulting in smooth velocity models suitable for migration of targets with moderately complex overburden, this work has the emphasis on using diffracted contributions in the wavefield for velocity inversion. Based on recently formulated diffraction symmetries, we motivate a two-step strategy, in which tomographic models gained via application to reflection data are subsequently refined using diffractions. Simple and complex synthetics, as well as an industrial field data example confirm the general finding that diffraction-based NIP tomography can lead to increased lateral resolution in the velocity inversion.

INTRODUCTION

The estimation of seismic velocities plays a central role in physically characterizing the Earth's interior on scales ranging from the exploration of hydrocarbon reservoirs in local regimes of the crust up to global investigations of the Earth's deeper mantle and core (e.g., Romanowicz, 2003). Besides their potential to answer fundamental geodynamical questions, seismic velocity models are also needed for the migration of recorded seismic data to the depth domain, which leads to structurally rich images of back-scattering impedance contrasts in the subsurface (Claerbout, 1970). In recent years, the direct inversion of full broadband waveforms has been emerging to become the primary tool for inferring the velocity structure with the highest possible resolution (Tarantola, 1984). Although being based on principles, which were already defined in the eighties, full-waveform inversion is still computationally highly demanding and in 3D can only be afforded by processers with access to high-performance computing facilities (e.g., Virieux and Operto, 2009). In addition, current implementations still mostly have to rely on large-offset acquisitions of diving waves with low frequencies or reasonably accurate starting velocity models to ensure stable convergence to the global misfit minimum (Virieux and Operto, 2009). The established process of depth migration, in turn, is designed to provide structural images of high resolution by focusing the back-scattered, reflected and diffracted contributions of the excited wavefield even at principally small source-receiver offsets. In contrast to full-waveform inversion, this method performs well for comparably smooth models with less detail in the velocity structure (e.g., Yilmaz, 2001).

While for full-waveform inversion and depth migration, sources and receivers, in principle, do not have to be densely distributed, stabilized tomographic inversion techniques exist, which make use of the redundancy in data recorded with dense source and receiver arrays, which are typical in seismic hydrocarbon exploration (Billette and Lambaré, 1998; Duveneck, 2004). These techniques can be formulated either in

the pre- or in the poststack domain and rely on the local coherence of the recorded wavefield. Prestack stereotomography approximates the wavefield's traveltimes, and, in addition to conventional traveltime tomography, its local slopes in the inversion (Billette and Lambaré, 1998). While this local description, in principle, allows for a high resolution in the inverted models, the poststack approach offers the benefits of a decreased noise level and data reduction, which can help to speed up and stabilize the process (Lavaud et al., 2004). The multi-dimensional common-reflection-surface (CRS) stack (Jäger et al., 2001) is a tool, which not only aims at optimally utilizing the redundancy in the data, but also automatically extracts valuable first- and second-order wavefield attributes, which can be used directly for a data-driven velocity inversion (Duveneck, 2004). In contrast to prestack stereotomography, this so-called NIP tomography is based on a second-order symmetry of the kinematics of the wavefield in the common-midpoint (CMP) gather, which can be expressed by an auxiliary one-way wave originating at the normal-incidence point (NIP) of the central ray (Hubral, 1983).

While previous applications had a strong emphasis on reflected events (Duveneck, 2004; Dümmong et al., 2008), recent works indicate that for diffractions, poststack attributes can be used to accurately describe the full kinematics of the prestack wavefield (Schwarz et al., 2014a; Bauer et al., 2014), which suggests a potential for increased resolution and stability of NIP tomography. In this work, we make use of the non-Snell scattering contributions in the data for obtaining better-resolved velocity models than with conventional applications, which are generally reflection-based. Starting with simple synthetic examples, we find support of the recently formulated diffraction symmetry, which can also be confirmed in the complex and challenging setting of the 2004 BP velocity benchmark (Billette and Brandsberg-Dahl, 2005). Concluding this paper, we apply a two-step strategy, comprising a sequential application of NIP tomography first to reflection- and then to diffraction-only industrial field data, acquired in the Eastern Mediterranean offshore Israel, which reveals the potential of increased resolution of diffraction-based inversion for a complex salt geometry.

COMMON-REFLECTION-SURFACE STACK

NIP tomography is based on kinematic wavefield attributes, which are obtained during the zero-offset (ZO) common-reflection-surface (CRS) stack (Jäger et al., 2001), in which a zero-offset section is simulated in a data-driven way. The ZO CRS stack is a multi-parameter stacking technique, which takes into account traces along a stacking surface in both offset and midpoint direction around a central midpoint x_0. Thus, the signal-to-noise ratio in the resulting zero-offset section can be significantly improved without providing any prior model information except the near-surface velocity. The CRS stacking operator depends on three parameters, which can be described in terms of the kinematic wavefield attributes α, R_{NIP} and R_N (Hubral, 1983). The attributes R_{NIP} and R_N describe the wavefront curvatures of two ficticious waves, the NIP-wave and the normal wave. These ficticious waves are excited by a point source placed on the reflector's normal-incidence point (NIP) and an exploding reflector segment around the NIP, respectively. The third parameter α describes the emergence angle at the central midpoint x_0, at which the two ficticious waves emerge at the recording surface. In the case of a diffraction, R_{NIP} and R_N coincide and the NIP-wave is the actual wavefront of the diffraction. The hyperbolic zero-offset CRS stacking operator is given by (Jäger et al., 2001)

$$t_{\mathrm{ZO}}^2(\Delta x_m, h) = \left(t_0^{\mathrm{ZO}} + \frac{2\sin\alpha}{v_0}\Delta x_m \right)^2 + \frac{2t_0\cos^2\alpha}{v_0}\left(\frac{\Delta x_m^2}{R_N} + \frac{h^2}{R_{NIP}} \right) , \tag{1}$$

where $\Delta x_m = x_m - x_0$ is the displacement from the central midpoint x_0, h denotes the half-offset and v_0 the constant near-surface velocity. Although the hyperbolic traveltime operator (1) is the most common one, different moveout descriptions have been introduced in the past years, especially non-hyperbolic operators such as i-CRS (Schwarz et al., 2014b) or multifocusing (Gelchinsky et al., 1999). At each zero-offset sample (x_0, t_0), values for the three wavefield attributes are determined by coherence analysis using either a pragmatic approach and subsequent local optimization (Mann, 2002) or a global optimization scheme (Walda and Gajewski, 2015). Also conflicting dips can be considered by allowing more than one operator at each sample (Mann, 2002; Soleimani et al., 2009; Walda and Gajewski, 2015). Since the wavefield attributes obtained from the ZO CRS stack have a physical meaning, they can be exploited for further processing steps, such as diffraction separation (Dell and Gajewski, 2011) or the tomographic inversion

revisited in this paper (Duveneck, 2004). In the following section, we briefly review the basic ingredients and concepts of NIP tomography.

NIP TOMOGRAPHY

NIP tomography, introduced by Duveneck (2004), is an efficient tomographic approach, which is entirely based on the zero-offset CRS attributes α and R_{NIP} and provides smooth 2D isotropic velocity models. Previous to the inversion, independent data points are picked in a data-driven way in the CRS semblance section by taking into account stack amplitudes and attribute values. During the tomographic inversion, rays are propagated through the model starting from the picked locations with the respective attribute values. The velocity model is updated according to the criterion that in a correct model, all considered NIP-waves focus at zero traveltime.

Input data and model

The input data for the inversion is a certain number of independent points, which are picked automatically in the zero-offset CRS results based on their coherence and a number of predefined constraints. Each pick is defined by its location on the recording surface x_0, its zero-offset traveltime t_0 and the wavefield attributes associated to the picked event, α and R_{NIP} (see Figure 1(b)). Instead of α and R_{NIP}, NIP tomography considers the one-way zero-offset traveltime,

$$T_0 = \frac{t_0}{2} \,, \tag{2}$$

the horizontal slowness of the normal ray,

$$p_{x_0} = \frac{\sin\alpha}{v_0} \,, \tag{3}$$

and the second derivative of the traveltime in a CMP-gather,

$$M_{NIP} = \frac{\cos^2\alpha}{v_0 R_{NIP}} \,, \tag{4}$$

where v_0 is the near-surface velocity given during the zero-offset CRS processing. Thus, the input data for the inversion algorithm is given by

$$(x_0, T_0, p_{x_0}, M_{NIP})_i \quad \text{with} \quad i = 1, \ldots, n_{picks} \quad , \tag{5}$$

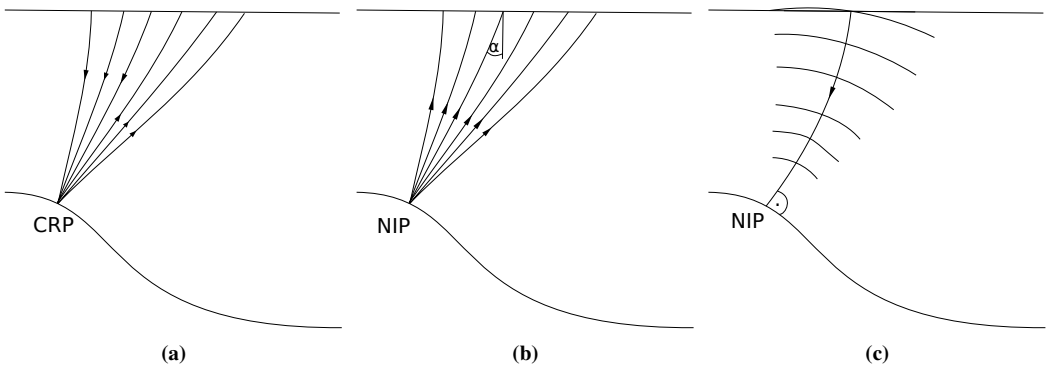

Figure 1: (a) Ray trajectories pertaining to one common-reflection-point (CRP) in the subsurface, (b) the ficticious NIP-wave excited by a point source placed on the reflector's normal-incidence-point (NIP), which emerges at the surface with the angle α, (c) in a correct model, the back-propagated NIP-waves should focus at zero time.

where n is the total number of picked data points. Each point i can be associated with a common-reflection-point (CRP) in the subsurface (see Figure 1(a)). In theory, checking if the back-propagated NIP-waves starting from x_0^i with $p_{x_0}^i$ for all picks focus at $T_0^i = 0$ is a valid condition for the inversion (see Figure 1(c)). However, we have to take into account that the data might be affected by errors in order to ensure a stable inversion. Therefore, at every CRP associated to one data point i, a ray is started in the subsurface by dynamic ray tracing (Duveneck, 2004). During this process, the true subsurface positions $(x, z)_i$ and the takeoff angles θ_i of the rays must be considered a part of the model, because they are unknown. In order to find the optimum velocity model, NIP tomography minimizes the misfit between measured and modeled values $(x_0, T_0, p_{x_0}, M_{NIP})_i$. Billette and Lambaré (1998) used a similar approach for stereotomography, which is a tomographic inversion method working in the prestack domain.

For the description of the smooth velocity model, NIP tomography uses 2D B-splines,

$$v(x,z) = \sum_{j=1}^{n_x} \sum_{k=1}^{n_z} v_{jk} \beta_j(x) \beta_k(z) \;, \tag{6}$$

where n_x and n_z are the total number of knots in x and z-direction, respectively. Accordingly, the model is defined by the B-spline coefficients v_{jk} and the coordinates and ray takeoff angles related to the picked data points,

$$\begin{aligned} (x, z, \theta)_i \quad &\text{with} \quad i = 1, \ldots, n_{picks} \quad , \\ v_{jk} \quad &\text{with} \quad (j,k) = (1,1), \ldots, (n_x, n_z) \; . \end{aligned} \tag{7}$$

In order to obtain the desired optimum velocity model, the inverse problem has to be solved iteratively. This process will be described in the following section.

Solution of the inverse problem

In order to solve the inverse problem, the algorithm has to find a model vector $\mathbf{m}$, which minimizes the misfit between a data vector $\mathbf{d}$ and the corresponding modeled values $\mathbf{d}_{\text{mod}} = \mathbf{f}(\mathbf{m})$ (Duveneck, 2004), where the model vector $\mathbf{m}$ contains all model components (7), the data vector $\mathbf{d}$ consists of all picked data points (5) and $\mathbf{f}$ is a nonlinear operator, which, in the case of NIP tomography, symbolizes the dynamic ray tracing carried out in the model. The presented inversion algorithm tries to minimize a cost function $\Psi(\mathbf{m})$ by using the least-squares norm (Paige and Saunders, 1982; Tarantola, 2005) as a measure of misfit. The cost function is given by

$$\Psi(\mathbf{m}) = \frac{1}{2} \|\mathbf{d} - \mathbf{f}(\mathbf{m})\|_D^2 = \frac{1}{2} \Delta\mathbf{d}^T(\mathbf{m}) \mathbf{C}_D^{-1} \Delta\mathbf{d}(\mathbf{m}) \;, \tag{8}$$

where $\Delta\mathbf{d}(\mathbf{m}) = \mathbf{d} - \mathbf{f}(\mathbf{m})$. The matrix $\mathbf{C}_D^{-1}$ is symmetric and positive definite. It weights the different data components during the calculation of Ψ. Due to the nonlinearity of the operator $\mathbf{f}$, the inverse problem is solved iteratively by locally linearizing $\mathbf{f}(\mathbf{m})$ around the current model vector. For this, the Fréchet derivatives of $\mathbf{f}$ are needed, which can be calculated during forward modeling (Farra and Madariaga, 1987). In order to facilitate a stable inversion, the requirement of a smooth velocity model is implemented as an additional constraint by minimizing its second derivatives. This results in an additional term in the cost function,

$$\Psi(\mathbf{m}) = \frac{1}{2} \Delta\mathbf{d}^T(\mathbf{m}) \mathbf{C}_D^{-1} \Delta\mathbf{d}(\mathbf{m}) + \frac{1}{2} \epsilon'' \mathbf{m}_{(v)}^T \mathbf{D}'' \mathbf{m}_{(v)} \;, \tag{9}$$

where $\mathbf{m}_{(v)}$ is the part of the model vector $\mathbf{m}$ containing the velocity coefficients. The additional term contains the integral

$$\mathbf{m}_{(v)}^T \mathbf{D}'' \mathbf{m}_{(v)} = \int_x \int_z \epsilon_{xx} \left(\frac{\partial^2 v(x,z)}{\partial x^2} \right)^2 + \epsilon_{zz} \left(\frac{\partial^2 v(x,z)}{\partial z^2} \right)^2 + \epsilon v^2(x,z) dx dz \;, \tag{10}$$

where the factors ϵ_{xx} and ϵ_{zz} are used for weighting the contributions of the corresponding second derivatives and ϵ is a weighting factor for the velocity itself. Since there is no physical reason to minimize the

velocity itself, ϵ should be chosen much smaller than ϵ_{xx} and ϵ_{zz}. The additional term may be added in order to ensure that the matrix $\mathbf{D}''$ is positive definite. For the explanation of the matrix $\mathbf{D}''$ and a more detailed description of the solution of the inverse problem we refer to the work of Duveneck (2004).

After setting up an initial velocity model, defined by a constant vertical velocity gradient or a given starting model, kinematic ray tracing for each picked data point $(x_0, T_0, p_{x_0}, M_{NIP})_i$ yields the corresponding coordinates $(x, z, \theta)_i$ in the model. As a next step, the algorithm performs dynamic ray tracing in the upward direction until the rays, which are started at $(x, z)_i$ with the angle θ_i, reach the measurement surface. The updated model for the n-th iteration is then given by $\mathbf{m}_{n+1} = \mathbf{m}_n + \lambda\Delta\mathbf{m}$, where $0 < \lambda \leq 1$. In this model, new data values are obtained from dynamic ray tracing and the cost function (9) is calculated. If its value decreases with respect to the previous iteration, the next iteration is started. Otherwise, the factor λ is decreased and the cost function is recalculated. If a minimum of the cost function is reached, the calculation is stopped.

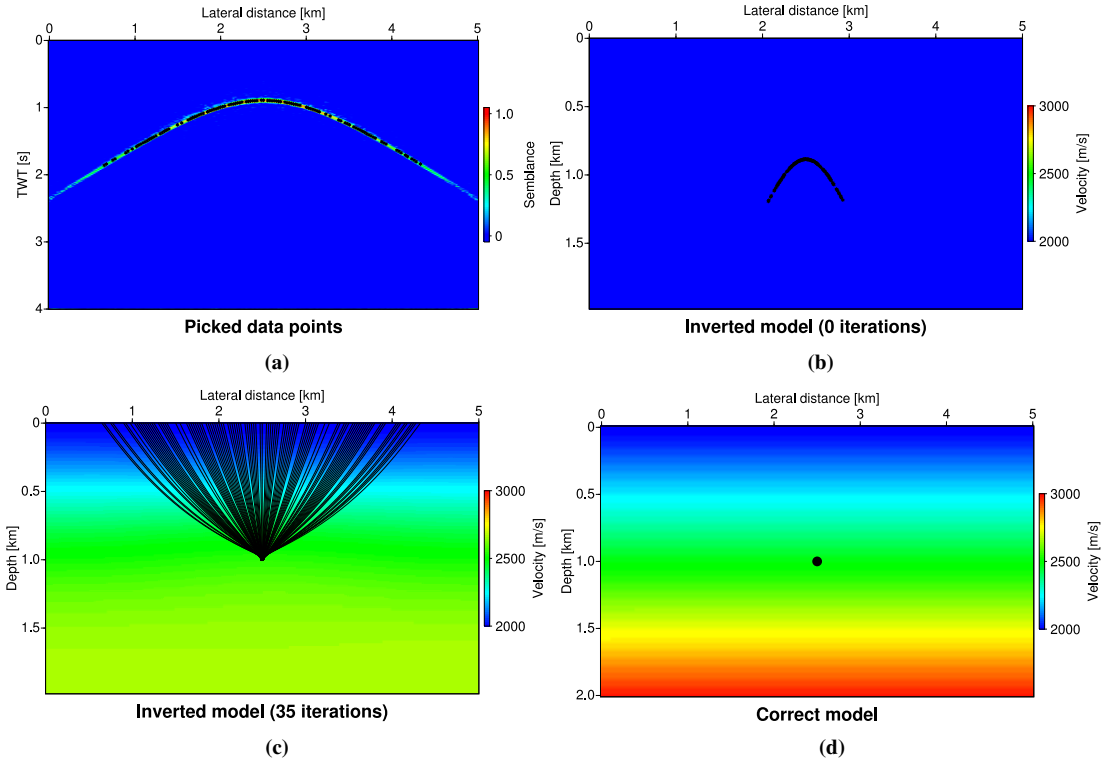

Figure 2: Results for simple diffraction data containing only one event. (a) Data points picked in the ZO CRS semblance section, (b) starting model for the inversion with initial starting points of the rays, (c) inverted model with final starting points of the rays and corresponding trajectories, (d) correct velocity model with diffractor indicated by a black dot.

SIMPLE DIFFRACTION DATA

In previous studies (Duveneck, 2004; Meier, 2007; Dümmong et al., 2008), NIP tomography has been applied based on input data points picked on reflections. However, diffraction events possess properties, which make them an interesting target for NIP tomography. Whereas in the case of a reflection, the NIP-wave emerges from a hypothetical point source placed on the reflector's normal-incidence point, in the case of a diffraction, the NIP-wave is excited by the diffractor itself and therefore, R_{NIP} describes the actual wavefront of the diffraction. Furthermore, diffractions imply better illumination than reflections, because a point diffractor scatters an incoming wave into all directions and thus, contributions stemming from the same diffractor can be recorded within a large part of the recording surface. This means that the rays corresponding to just one diffraction may already travel through a significant part of the model. In

addition, the proximity of the starting coordinates of all rays connected to one diffraction serves as a strong quality criterion for the inverted model.

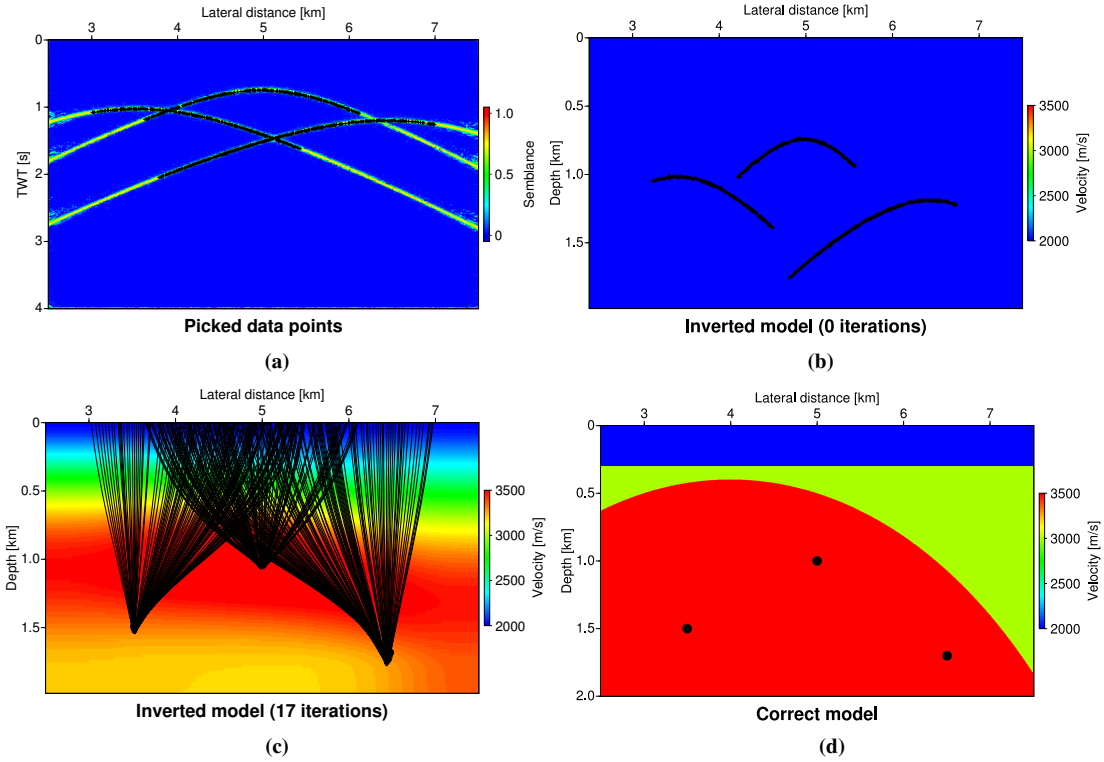

Figure 3: Results for simple data based on a hetereogeneous model containing three point diffractors. (a) Data points picked in the ZO CRS semblance section, (b) starting model for the inversion with initial starting points of the rays, (c) inverted model with final starting points of the rays and corresponding trajectories, (d) correct velocity model with the diffractors indicated by black dots.

In order to test NIP tomography with diffraction-only data under controlled conditions, we applied it to a simple dataset containing one diffraction based on a model with a constant vertical velocity gradient of $0.5\,\mathrm{s}^{-1}$. The results are displayed in Figure 2, where Figure 2(a) shows the data points, which were picked in a data-driven way in the zero-offset CRS semblance section also taking into account the CRS stack and the attributes α and R_{NIP}. As expected, all picks lie on the diffraction hyperbola. Figure 2(b) shows the initial velocity model for the tomographic inversion, which merely consists of the near-surface velocity v_0 and no initial vertical velocity gradient. The black asterisks indicate the starting locations of the rays. In a correct velocity model, these locations should coincide for all rays pertaining to the same diffractor. Accordingly, Figure 2(c) shows the inverted model using NIP tomography, the final starting coordinates of the rays and the corresponding ray trajectories. A comparison of the inverted model with the correct one displayed in Figure 2(d) reveals a good agreement in those parts of the model illuminated by the rays. In addition, although all picked data points are treated independently by the algorithm, the final starting locations of the rays are confined to the same depth point, which coincides with the actual position of the diffractor indicated by the black dot in the correct model. In this example, we used 18×18 B-spline knots with a spacing of 250 m in x-direction and 100 m in z-direction for the tomographic inversion.

As a next step, we applied the same workflow to a simple dataset based on a model, which contains both vertical and lateral heterogeneity and three point diffractors at different locations in the subsurface. The tomographic inversion was done with the same knot spacing as in the previous example. Figure 3 shows the results of this application. In Figure 3(a), the asterisks indicate the picked data points in the zero-offset CRS semblance section. In this case, data points with $\alpha > 30^\circ$ were neglected for a better inversion result, because the estimation of the wavefield curvature R_{NIP} is less accurate on the flanks of a diffraction

hyperbola. As in the previous example, the initial model for the tomographic inversion consisted in the constant near-surface velocity v_0, as displayed in Figure 3(b), where the starting locations of the rays again indicate the wrong velocity model. The result of the inversion is displayed in Figure 3(c) including the final starting coordinates of the rays and their trajectories. In the inverted model, the ray starting locations are confined nicely to three distinct depth points, only the ones pertaining to the deepest one reveal some inaccuracies. The correct model shown in Figure 3(d) reveals that the inverted depth points coincide very well with the true diffractor positions. However, the inverted model shows some differences compared to the true one. As before, the ray coverage in Figure 3(c) indicates, in which parts of the model no reliable result can be expected.

COMPLEX DATA

2004 BP velocity benchmark

In order to test the NIP tomography in a more complex setting, we applied it to the 2004 BP velocity benchmark, which is a complex synthetic dataset introduced by Billette and Brandsberg-Dahl (2005). It is based on a velocity model which contains complex salt geometries to the left and in the center and a relatively shallow mud volcano structure surrounded by an increasing vertical velocity gradient to the right of the profile line. The data was modeled including free-surface multiples. Accordingly, in order to avoid the picking of multiples, they had to be muted in the input data. For that, we applied a simple algorithm to attenuate all events with water velocity. Additionally, we separated diffractions from reflections by applying a CRS-attribute-based weighting function (Dell and Gajewski, 2011) to the input semblance section. In Figure 4(a), all picked data points in the zero-offset CRS semblance section are displayed. Events found in the reflection-only section are indicated by white asterisks and events picked in the diffraction-only section are indicated by black asterisks.

As a next step, we applied NIP tomography using only the picked reflection events as input. We used a grid of 34×12 B-spline knots with a spacing of 2 km in x and 1 km in z-direction and a small initial vertical velocity gradient of $0.05\,\mathrm{s}^{-1}$. The resulting model based on reflection-only data with the final ray starting locations is displayed in Figure 4(b). Although it does not contain detailed structures, the inverted model resembles the laterally increasing vertical velocity gradient, which can be observed in the correct velocity model (see Figure 4(d)). In the left part of the model, the velocities stay close to the initial gradient, since there are no picks from the subsalt region. As a consequence, neither the velocity gradient, nor the salt bodies can be resolved. In the next step, we carried out the tomographic inversion solely based on the diffraction picks and using the reflection result as initial model. The inverted model is shown in Figure 4(c). Overall, the differences in the velocity distribution compared to the reflection result are small. However, in some parts of the model, we observe an increased resolution. For example, the large velocity gradient around the mud volcano structure to the right of the model is better resolved. Also, there are changes in the left part of the model, where the salt body is located, because this part is dominated by strong top-of-salt diffractions.

Figure 4(d) shows the correct velocity model overlain with the final starting locations of the rays corresponding to the reflection picks (white) and the diffraction picks (black). In particular, the starting locations of the rays connected to the diffractions coincide very well with the top of the salt bodies to the left and in the center of the model. Although the algorithm treats all picked data points independently, picks pertaining to the same diffraction (compare Figure 4(a)) focus at their corresponding depth point at the top of the salt structures. This promising observation reveals both the potential and the importance of diffraction-based tomographic inversion.

Marine field data

Finally, we applied the same workflow to a marine field dataset recorded by TGS in the Levantine Basin, which is located in the Eastern Mediterranean offshore Israel. In previous studies, Meier (2007) and Dümmong et al. (2008) applied both NIP tomography and prestack stereotomography (Billette and Lambaré, 1998) to various lines acquired in the same region. The profile considered in this work is characterized by pronounced salt roller structures in the left part (Hübscher and Netzeband, 2007).

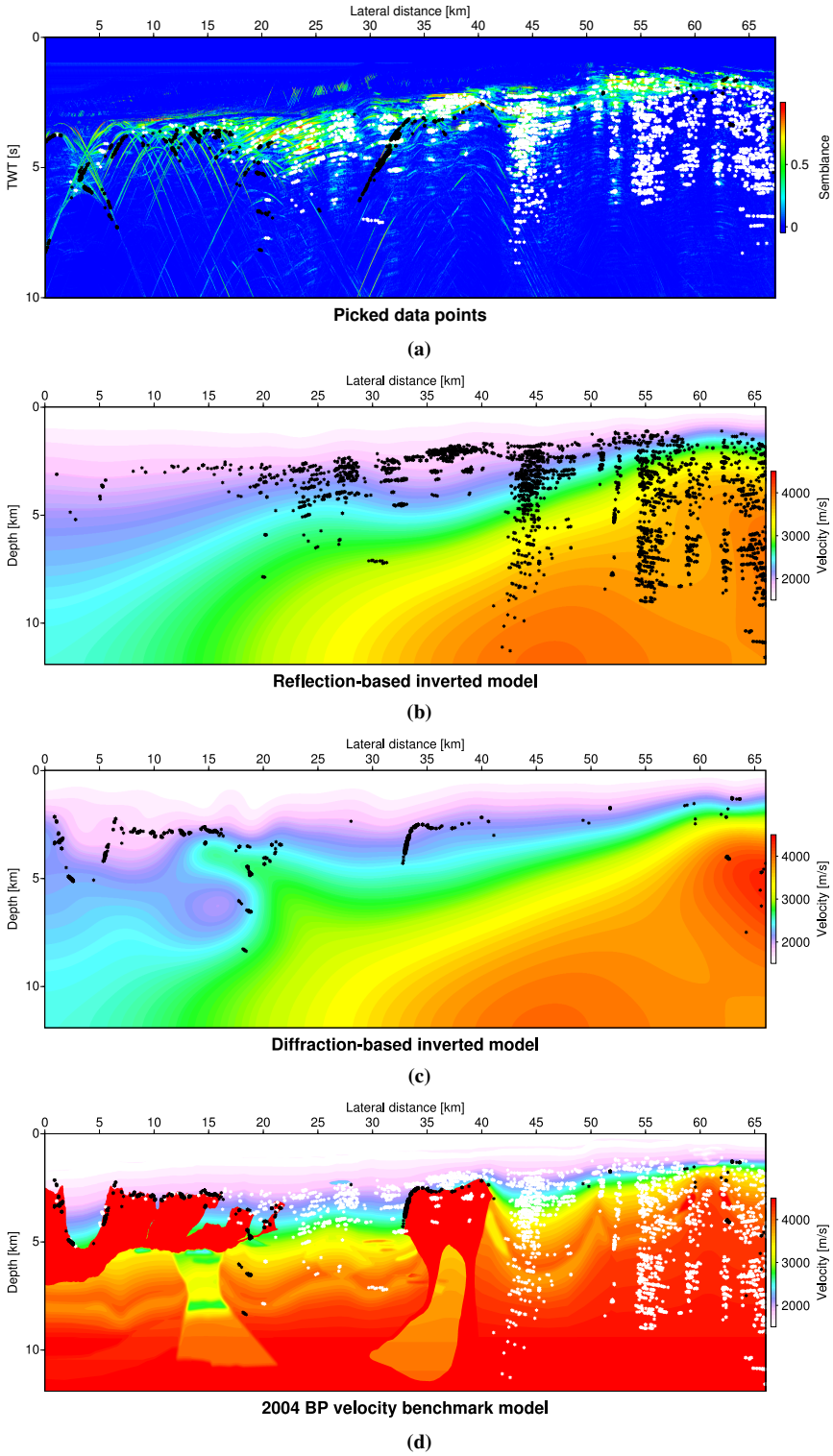

Figure 4: Results for the 2004 BP velocity benchmark. (a) Picks of reflections (white) and diffractions (black) in the multiple-free ZO CRS semblance section, (b) inverted model using only reflection picks with final starting points of the rays, (c) inverted model using (b) as initial model and only diffraction picks with final starting points of the rays, (d) correct velocity model with final ray starting locations of reflections (white) and diffractions (black).

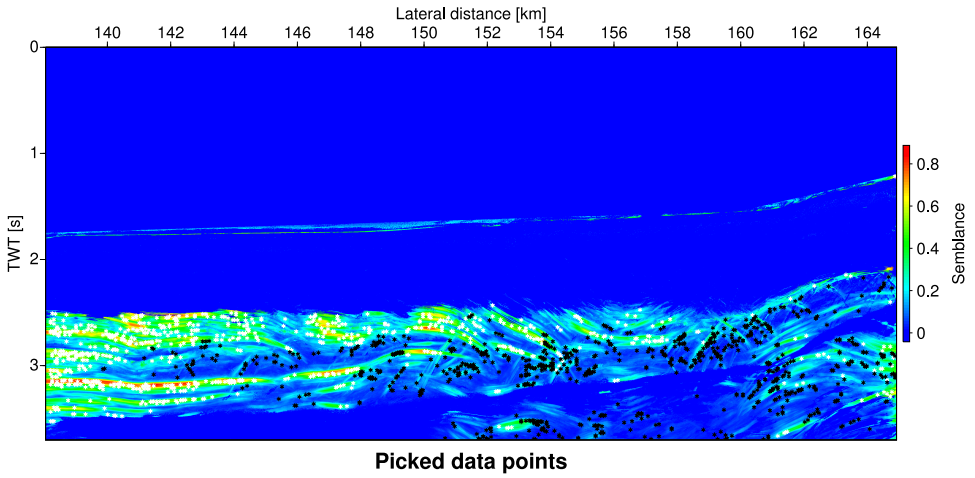

(a)

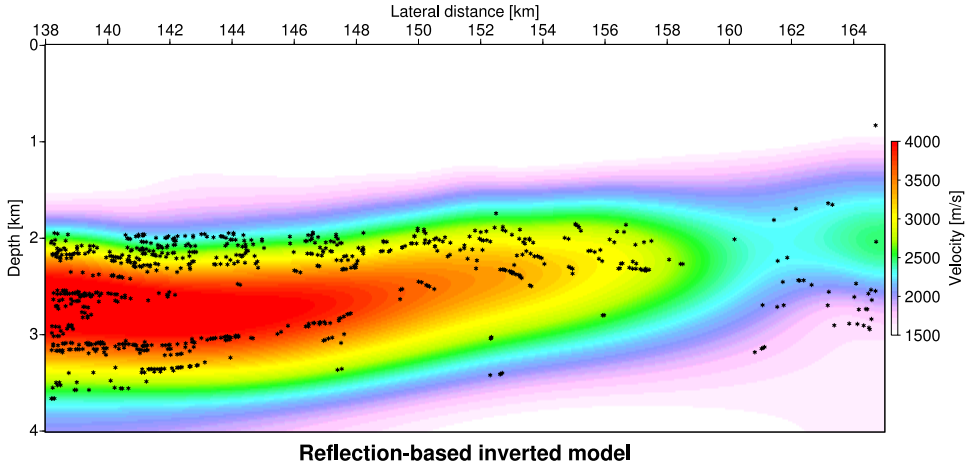

(b)

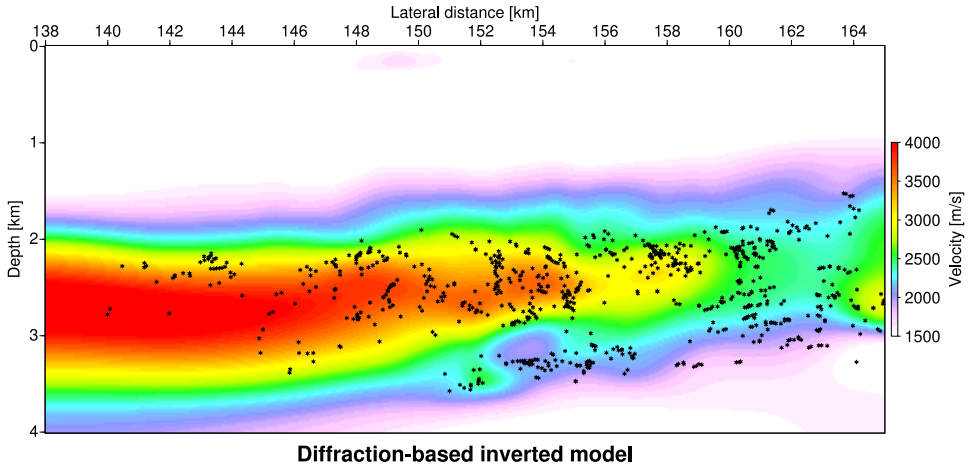

(c)

Figure 5: Marine field data results. (a) Picks of reflections (white) and diffractions (black) in the multiple-free ZO CRS semblance section, (b) inverted model using only reflection picks with final starting points of the rays, (c) inverted model using (b) as initial model and only diffraction picks with final starting points of the rays.

As in the previous example, the picking of events was carried out in a zero-offset CRS semblance section, where all events related to the water velocity were muted, and reflections and diffractions were separated and picked independently. Figure 5(a) shows the picked data points in the zero-offset CRS semblance section. The reflection and diffraction picks are indicated by white and black asterisks, respectively.

For the inversion, we used a grid of 54×41 knots with a spacing of 500 m in x and 100 m in z-direction and, as in the previous example, a small initial vertical velocity gradient of $0.05\,\mathrm{s}^{-1}$. The inverted model based on the reflection-only picks with the corresponding final ray starting locations is displayed in Figure 5(b). It contains a high velocity zone in the left part, which is in agreement with the salt geometry present in the region (see also Hübscher and Netzeband, 2007; Dümmong et al., 2008). As in the previous example, we used the result obtained with reflection picks as initial model for the second step, in which we inverted for the data points picked in the diffraction-only section. The resulting model of the proposed two-step strategy is shown in Figure 5(c). While the general velocity distribution does not change, the data points connected to diffractions seem to enhance the resolution in those parts of the model, which are well illuminated.

CONCLUSIONS AND OUTLOOK

In this paper, we revisited the largely data-driven process of NIP tomography as an efficient tool to infer the seismic velocity structure of the subsurface, which does not require a priori velocity information. With special emphasis on non-Snell scattering, we illustrated by means of a simple synthetic example that the use of diffracted contributions can enhance the resolution of the inverted models. Application to the complex 2004 BP velocity benchmark dataset not only confirmed these findings for a more complex setting, it also showed that the suggested two-step strategy of refining smooth models gained through reflection data by systematically taking even weak-amplitude diffractions into account is a promising approach. In the final part of this work, this two-step strategy led to a reliable detection of the salt but also to an increased resolution of the inverted velocity model compared to the conventional result, gained by favoring reflections.

NIP tomography is an efficient and stable tool to obtain smooth velocity models without having to interact with the full prestack data volume, but merely with the results from zero-offset CRS processing. While this leads to a certain robustness with respect to, e.g., random noise, errors made in the coherence and parameter estimation can have significant impact on the quality of the inversion. Therefore, further improvement of the CRS stack, by utilizing global optimization strategies (e.g., Walda and Gajewski, 2015) or by incorporating more accurate moveout approximations that are better suited for diffractions (e.g., Schwarz et al., 2014b), as well as the design of more sophisticated diffraction filters is of central importance to improve NIP tomography for diffractions. In addition, the direct incorporation of the diffraction symmetry revealed by Schwarz et al. (2014a) and first utilized by Bauer et al. (2014) into the inversion should lead to a better constrained and more stable inversion.

ACKNOWLEDGMENTS

This work was kindly supported by the sponsors of the *Wave Inversion Technology (WIT) Consortium*, Hamburg, Germany. We thank the applied seismics group at the University of Hamburg for continuous discussion, Billette and Brandsberg-Dahl (2005) for providing the 2004 BP velocity benchmark dataset and TGS for providing the marine field data.

REFERENCES

Bauer, A., Schwarz, B., and Gajewski, D. (2014). From ZO to CO with diffractions: Theory. *18th Annual WIT report*.

Billette, F. and Brandsberg-Dahl, S. (2005). The 2004 BP velocity benchmark. In *67th EAGE Conference and Exhibition*.

Billette, F. and Lambaré, G. (1998). Velocity macro-model estimation from seismic reflection data by stereotomography. *Geophysical Journal International*, 135(2):671–690.

Claerbout, J. (1970). Coarse grid calculations of waves in inhomogeneous media with application to delineation of complicated seismic structure. *Geophysics*, 35(3):407–418.

Dell, S. and Gajewski, D. (2011). Common-reflection-surface-based workflow for diffraction imaging. *Geophysics*, 76(5):S187–S195.

Dümmong, S., Meier, K., Gajewski, D., and Hübscher, C. (2008). Comparison of prestack stereotomography and NIP wave tomography for velocity model building: Instances from the Messinian evaporites. *Geophysics*, 73(5):VE291–VE302.

Duveneck, E. (2004). Velocity model estimation with data-derived wavefront attributes. *Geophysics*, 69(1):265–274.

Farra, V. and Madariaga, R. (1987). Seismic waveform modeling in heterogeneous media by ray perturbation theory. *Journal of Geophysical Research: Solid Earth (1978–2012)*, 92(B3):2697–2712.

Gelchinsky, B., Berkovitch, A., and Keydar, S. (1999). Multifocusing homeomorphic imaging: Part 1. basic concepts and formulas. *Journal of Applied Geophysics*, 42(3):229–242.

Hubral, P. (1983). Computing true amplitude reflections in a laterally inhomogeneous earth. *Geophysics*, 48:1051–1062.

Hübscher, C. and Netzeband, G. (2007). Evolution of a young salt giant:: The example of the messinian evaporites in the levantine basin. In Wallner, M., Lux, K.-H., Minkley, W., and Hardy, J. H., editors, *The mechanical behaviour of salt*, pages 175–184. Taylor & Francis, London.

Jäger, R., Mann, J., Höcht, G., and Hubral, P. (2001). Common-reflection-surface stack: Image and attributes. *Geophysics*, 66:97–109.

Lavaud, B., Baina, R., and Landa, E. (2004). Automatic robust velocity estimation by poststack stereotomography. In *SEG Expanded Abstracts*. Society of Exploration Geophysicists.

Mann, J. (2002). *Extensions and applications of the common-reflection-surface stack method*. PhD thesis, University of Karlsruhe.

Meier, K. (2007). Velocity model building: A comparison between prestack stereotomography and nip-wave tomography. diploma thesis, University of Hamburg.

Paige, C. C. and Saunders, M. A. (1982). LSQR: An algorithm for sparse linear equations and sparse least squares. *ACM Transactions on Mathematical Software (TOMS)*, 8(1):43–71.

Romanowicz, B. (2003). Global mantle tomography: progress status in the past 10 years. *Annual Review of Earth and Planetary Sciences*, 31(1):303–328.

Schwarz, B., Vanelle, C., and Gajewski, D. (2014a). From zero-offset to common-offset with diffractions. In *76th EAGE Conference and Exhibition - Workshops*.

Schwarz, B., Vanelle, C., Gajewski, D., and Kashtan, B. (2014b). Curvatures and inhomogeneities: an improved common-reflection-surface approach. *Geophysics*, 79(5):S231–S240.

Soleimani, M., Piruz, I., Mann, J., and Hubral, P. (2009). Solving the problem of conflicting dips in common-reflection-surface (CRS) stack. In *1st International Petroleum Conference & Exhibition*.

Tarantola, A. (1984). Inversion of seismic reflection data in the acoustic approximation. *Geophysics*, 49(8):1259–1266.

Tarantola, A. (2005). *Inverse problem theory and methods for model parameter estimation*. SIAM.

Virieux, J. and Operto, S. (2009). An overview of full-waveform inversion in exploration geophysics. *Geophysics*, 74(6):WCC1–WCC26.

Walda, J. and Gajewski, D. (2015). Common-reflection-surface stack improvement by differential evolution and conflicting dip processing. In *SEG Technical Program Expanded Abstracts 2015*, pages 3842–3847. Society of Exploration Geophysicists.

Yilmaz, Ö. (2001). *Seismic data analysis*, volume 1. Society of Exploration Geophysicists, Tulsa.